Solar RRL
www.solar-rrl.com

Monolithic Perovskite/Silicon Tandem Solar Cells Fabricated Using Industrial p-Type Polycrystalline Silicon on Oxide/Passivated Emitter and Rear Cell Silicon Bottom Cell Technology

Silvia Mariotti, Klaus Jäger, Marvin Diederich, Marlene S. Härtel, Bor Li, Kári Sveinbjörnsson, Sarah Kajari-Schröder, Robby Peibst, Steve Albrecht, Lars Korte, and Tobias Wietler**

Combining a perovskite top cell with a conventional passivated emitter and rear cell (PERC) silicon bottom cell in a monolithically integrated tandem device is an economically attractive solution to boost the power conversion efficiency (PCE) of silicon single-junction technology. Proof-of-concept perovskite/silicon tandem solar cells using high-temperature stable bottom cells featuring a polycrystalline silicon on oxide (POLO) front junction and a PERC-type passivated rear side with local aluminum-p^+ contacts are reported. For this PERC/POLO cell, a process flow that is compatible with industrial, mainstream PERC technology is implemented. Top and bottom cells are connected via a tin-doped indium oxide recombination layer. The recombination layer formation on the POLO front junction of the bottom cell is optimized by postdeposition annealing and mitigation of sputter damage. The perovskite top cell is monolithically integrated in a p–i–n junction device architecture. Proof-of-concept tandem cells demonstrate a PCE of up to 21.3%. Based on the experimental findings and supporting optical simulations, major performance enhancements by process and layer optimization are identified and a PCE potential of 29.5% for these perovskite/silicon tandem solar cells with PERC-like bottom cell technology is estimated.

1. Introduction

Silicon solar cells have been the working horses of the photovoltaic industry for decades. Continuous technological progress has led to increases in power conversion efficiency (PCE) and driven the levelized cost of electricity (LCOE) down to 1.33 \$ct kWh^{-1} in sunny regions such as Chile.[1] To continue this success story, the combination of a silicon bottom solar cell with a low-cost, wide-bandgap top cell into a tandem device is perceived as an intriguing technological path toward cost-effective multijunction solar cells with PCEs beyond the silicon single-junction efficiency limit of 29.5%.[2] In particular, perovskite/silicon tandem solar cells have triggered impressive research and development that peaked in devices with PCEs approaching 30%.[3–5] However, as of late 2021, the majority of the reported monolithic perovskite/silicon tandem solar cells with highest PCE results rely on silicon heterojunction (SHJ) bottom cells, exploiting SHJ's high open-circuit voltages (see, e.g., Jost et al. for a recent review).[6] The

S. Mariotti, M. S. Härtel, B. Li, K. Sveinbjörnsson, S. Albrecht, L. Korte
Young Investigator Group Perovskite Tandem Solar Cells
Helmholtz-Zentrum Berlin für Materialien und Energie GmbH
12489 Berlin, Germany
E-mail: korte@helmholtz-berlin.de

K. Jäger
Department Optics for Solar Energy
Helmholtz-Zentrum Berlin für Materialien und Energie GmbH
12489 Berlin, Germany

The ORCID identification number(s) for the author(s) of this article can be found under https://doi.org/10.1002/solr.202101066.

© 2022 The Authors. Solar RRL published by Wiley-VCH GmbH. This is an open access article under the terms of the Creative Commons Attribution License, which permits use, distribution and reproduction in any medium, provided the original work is properly cited.

DOI: 10.1002/solr.202101066

M. Diederich, S. Kajari-Schröder, R. Peibst, T. Wietler
Institute for Solar Energy Research (ISFH) GmbH
31860 Emmerthal, Germany
E-mail: wietler@isfh.de

M. S. Härtel, S. Albrecht
Fakultät Elektrotechnik und Informatik
Technische Universität Berlin
23, 10587 Berlin, Germany

R. Peibst
Institute of Electronic Materials and Devices
Leibniz University Hannover
30167 Hannover, Germany

few reports on monolithic perovskite/silicon tandem solar cells with silicon homojunction bottom cells use n-type silicon wafers with different rear side passivation and subcell integration strategies.[7–12] The highest PCE reported so far for such tandems on homojunction bottom cells is 23.0%.[11]

The leading silicon solar cell technology, however, is p-type passivated emitter and rear cell (PERC) with a market share of around 75% in 2020.[13] PERC technology is highly cost competitive and any (small) efficiency benefit of other c-Si technologies is roughly halved in a bottom cell for tandem applications. This results in an even smaller margin for related higher material costs, higher capital expenditure (CAPEX), etc. in tandem cells. The perovskite on PERC approach is therefore economically attractive compared with other perovskite/silicon tandem cell approaches.[14] Peibst et al. proposed an integration scheme that replaces the diffused phosphorous emitter of a PERC cell by an electron-collecting passivating polycrystalline silicon on oxide (POLO) junction.[15,16] The integration of highly doped and at least partly crystalline silicon on oxide layers as bottom cell front junctions in perovskite/silicon tandem cells has been demonstrated using p-type silicon layers on n-type wafers and n-type SiC_x layers on p-type wafers resulting in PCEs of 24.1%[12] and 25.1% ,[17] respectively. In the study by Nogay et al.,[17] a p-type SiC_x junction with tin-doped indium oxide (ITO) and silver layers formed the bottom cell rear contact. Up to now, the experimental demonstration of a perovskite–POLO–PERC tandem cell (in the following denoted as "3 P tandem cell") is still lacking.

Here, we report on a proof-of-concept 3 P tandem solar cell with a high-temperature stable bottom cell featuring a POLO front junction and PERC rear side. We implement a bottom cell process flow that is compatible with industrial, mainstream PERC technology. In particular, the active device area of our silicon bottom cell features all industrially relevant components such as p-type Czochralski (Cz) saw damage-etched (SDE) base material, in situ n-type-doped poly-Si layers on a wet chemically grown interfacial oxide, a fired Al_2O_3/SiN_x rear side passivation, as well as screen-printed and alloyed aluminum (Al) p^+ rear contacts. An ITO recombination layer links the bottom cell to the perovskite top cell, that is fabricated using a p–i–n device architecture, similar to the top cell used for tandem devices built on SHJs enabling the highest tandem efficiency.[3] First results show a PCE up to 21.3% for monolithic, 2-terminal perovskite–POLO–PERC tandem solar cells. We report on the major limitations of our proof-of-concept tandem device to support further efficiency enhancements as well as process optimization of this tandem concept. Based on our experimental findings and optical simulations, we identify major process enhancements and estimate a PCE potential of 29.5% for this tandem technology using mainstream silicon bottom cells.

2. Experimental Section

2.1. Bottom Cell Processing and Bottom Cell Characterization

Our bottom cells are fabricated at the Institute for Solar Energy Research (ISFH) and comprise all components of industrial PERC cells, except for the substitution of $POCl_3$ diffusion by low-pressure chemical vapor deposition (LPCVD) of in situ n^+-type p-doped poly-Si. We use p-type Ga-doped Cz wafers with M2 format (pseudosquare) wafers with 156.75 mm edge length, a diameter of 210 mm, and a base resistivity of 1.05 Ω cm. After saw damage removal, we grow a wet chemical interfacial oxide using ozone diluted in water. This last step easily blends into a conventional wet chemical cleaning sequence. We deposit in situ n^+-doped Si on both sides of the wafers by LPCVD. The formation of the n^+ POLO junctions includs crystallization, local oxide layer break-up, and impurity gettering in the n^+ POLO layers. It is performed at 840 °C and the final layer thickness of the n^+-doped poly-Si is 55 nm.

The top cell processing is at the moment restricted to an area of ≈1 cm^2 due to utilization of spin coating on small Si substrates. To match the active area of both subcells, we introduce two patterning steps of the bottom cell front side. The first one defines the n^+ POLO emitter in the active cell area and removes the n^+-doped poly Si on the rear side. Next, stacks of Al_2O_3 and SiN_x are deposited on both sides of the wafer. The rear-side 15 nm Al_2O_3/100 nm SiN_x stack serves for passivation just as in an industrial PERC cell. The front-side 10 nm Al_2O_3/40 nm SiN_x stack passivates the perimeter region around the active cell area (see **Figure 1**a). It also serves the rather fundamental purpose to stabilize the POLO junction passivation during the subsequent firing process and is therefore removed in the active area only after firing. The details of both the poly-Si and the Al_2O_3/SiN_x patterning processes are described in the supporting information together with a cross-sectional schematic of the bottom-cell process (see Figure S1.1, Supporting Information). Front-side patterning will become obsolete for scaled-up devices with active areas of both subcells being equivalent to the full wafer format. In a full-area industrial cell, a sacrificial H donor layer like the front-side Al_2O_3/SiN_x stack could be avoided by, for example, H plasma treatment after firing. However, firing of POLO junctions without any degradation is even possible at low firing belt velocities, which can make additional H supply unnecessary.[18]

After local ablation of the passivation stack on the rear side using a laser with 532 nm wavelength and pulses in the picosecond range, we screen print Al fingers on top of the laser contact openings. The wafers are fired in a conveyor belt furnace at 810 °C set point temperature with a belt speed of 7.2 m min^{-1}.

To analyze the quality of the bottom cells, we measure the implied current–voltage characteristics of the final bottom cells by injection-dependent infrared lifetime mapping (ILM).[19] We investigate the characteristics of the bottom cells after ITO sputtering and annealing by current density–voltage analysis (J–V) and illumination-dependent measurements of short-circuit current density (J_{SC}) and open-circuit voltage (V_{OC}), so-called $J_{SC}V_{OC}$ measurements.[20] Further details on the device characterization are given in the supplemental information.

2.2. Top Cell Processing and Tandem Cell Characterization

After shipping the bottom cells to Helmholtz-Zentrum Berlin für Materialien und Energie (HZB), they are treated with HF (2%, 2 min). Afterward, the 20 nm-thick ITO forming the recombination junction between the bottom and the top cell is sputtered. In an industrial cell process without a hydrogen-

© 2022 The Authors. Solar RRL published by Wiley-VCH GmbH

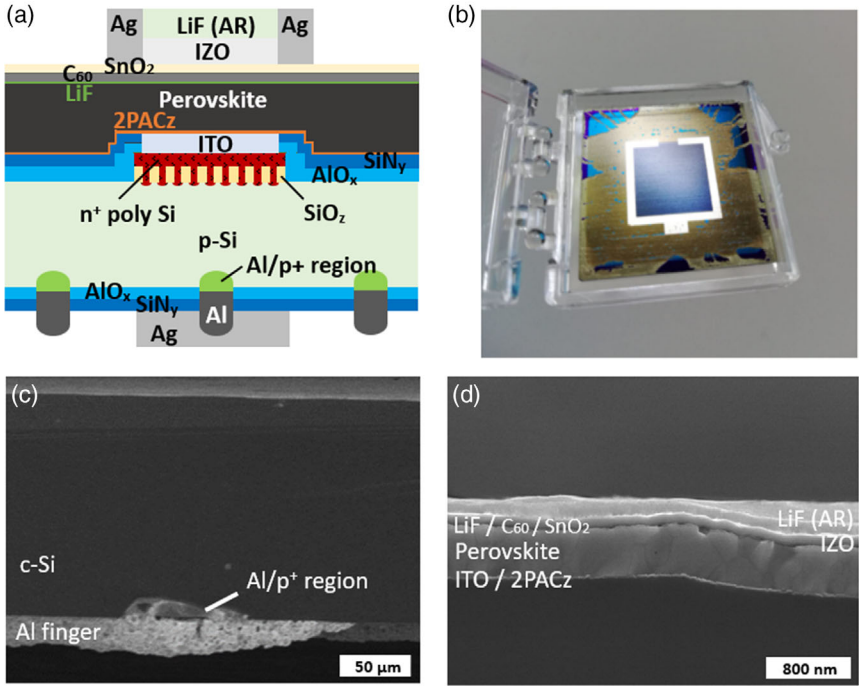


Figure 1. a) Cross-sectional schematics of the perovskite–POLO–PERC tandem solar cell and b) top-view photograph with an active area of ≈1 cm^2. Scanning electron microscopy (SEM) images of c) bottom cell and d) top cell of the tandem device. In (c) the POLO front junction and the rear-side passivation layer are not visible due to small magnification.

donating layer on top of poly-Si, a thin silicon oxide would possibly grow on the bare poly-Si surface. In this case, plasma etching prior to the deposition of the recombination layer or the hole transport layer (HTL) could be a solution. Here, we adjust the top device process to optimize the device performance. Since it is known that sputtering of a transparent conductive oxide (TCO) on top of poly-Si/c-Si contacts can yield degradation of the passivation quality,[21,22] we performe a postdeposition anneal (PDA) of the ITO recombination junction. We also apply a soft sputtering deposition technique as another way to mitigate sputtering damage, by reducing the plasma UV radiation on the substrate, increasing the path length of particles, and reducing the kinetic energy of the particles hitting the substrate.[22–24]

The perovskite top cell is fabricated in a p–i–n device architecture. This architecture is chosen to allow the fabrication of a perovskite/silicon tandem solar cell with a well-known top-cell device stack, also used for record perovskite/SHJ tandem devices.[3] We use the self-assembling monolayer (SAM) [2-(9 H-carbazol-9-yl)ethyl]phosphonic acid (2PACz) as a HTL. This SAM efficiently extractes holes from the perovskite and reduce nonradiative recombination losses at the interface.[25] Then, we spin coat the perovskite precursor layer, followed by an annealing step that leads to the formation of the photoactive perovskite crystal structure. Here, we use a triple-halide $CsFAPb(IBrCl)_3$ perovskite composition, similar to that reported by Xu et al.[26] and Lang et al.,[27] with a bandgap of 1.68 eV. While we use a spin-speed of 5000 rpm for the fabrication of perovskite single junctions, we adjusted the concentration to 1.4 M and the spin speed from 3500 to 5000 rpm when spin coating on bottom cells, to fine tune the average thickness of the wrinkled perovskite layer from roughly 560 nm to 470 nm to drive the current density of the top cell closer to current matching with the planar bottom cell (see Figure S2.1, Supporting Information). After perovskite annealing, we thermally evaporate an ultrathin layer of lithium fluoride (LiF) and 18 nm of C_{60}. In particular, LiF passivate defects at the perovskite/C_{60} interface, whereas C_{60} is used as the electron transport layer (ETL).[3] We then use atomic layer deposition (ALD) to apply a 20 nm SnO_2 buffer layer and sputter a 100 nm transparent conductive zinc-doped indium oxide (IZO) layer. Afterwards, a ring-shaped silver contact forming the front contact and a LiF antireflective coating are thermally evaporated. For comparison, perovskite single-junction devices with the structure glass/ITO/2PACz/Perovskite/LiF/C_{60}/SnO_2/Ag are processed in parallel to the tandems. Figure S2.2, Supporting Information, shows $J-V$ parameters of these single-junction devices with average PCE of about 19%. Finally, we add a silver (Ag) layer as optical reflector on the rear side of the bifacial $PERC^+$ bottom cell, with the aim of increasing the bottom cell J_{SC}. The active area of the tandem device was 1.01 cm^2. The layer stack of the tandem device together with a photograph of the finished tandem cell and cross-sectional scanning electron microscopy (SEM) images for top and bottom cells are shown in Figure 1.

The tandem cells were characterized using $J-V$, external quantum efficiency (EQE), and reflection measurements. Further details of the top cell process and device characterization are described in the Supporting Information.

© 2022 The Authors. Solar RRL published by Wiley-VCH GmbH

3. Results and Discussion

One major challenge for monolithic perovskite/silicon tandem solar cells is the recombination junction between both subcells.[28] ITO has a proven track record as one solution for integrating perovskite top cells onto SHJ bottom cells.[3] However, the passivation quality of POLO junctions can suffer from subsequent sputter deposition of TCO layers. In particular, this is the case if poly-Si is only a few tens of nanometers thin.[21,22] A PDA at temperatures around 300 °C can cure this sputtering damage.[29] Here, we anneal our devices in air after HF treatment and ITO sputtering up to 300 °C for 10 min.

The annealing step is crucial for the tandem device performance, as it helps to restore the bottom cell V_{OC}. **Figure 2**a shows the $J-V$ curves obtained from bottom cells with a 100 nm-thick sputtered ITO recombination layer and an evaporated Ag front contact without annealing and after PDA at 200 and 300 °C. Compared with the tandem devices, here we choose a thicker ITO layer for the experiments with Si single-junction cells to enhance the lateral conductivity of the front electrode. An example for a bottom cell with a 20 nm-thick ITO layer is shown in the supporting information. From the device characteristics, it is evident that the annealing process is essential to improve both FF and V_{OC}. The FF increases from 55.2% to 68.4% and V_{OC} increases from 644 to 677 mV after PDA treatment at 300 °C. $J-V$ and $J_{SC}V_{OC}$ measurements on similar cells after PDA at 350 °C corroborate these findings (see Figure S3.1, Supporting Information): The V_{OC} reaches 690 mV. From the $J_{SC}V_{OC}$ data, we extract a pseudo-fill factor of 81.3%, much higher than the FF from the $J-V$ curve. This indicates that the series resistance caused by the low lateral conductivity of the ITO layer limits the fill factors extracted from the $J-V$ measurements in Figure 2a and S3.1, Supporting Information. However, we will not discuss this further, because the lateral conductivity of this intermediate ITO layer does not limit the purely vertical transport in the full tandem device. We find that after PDA at temperatures above 300 °C, the bottom cell becomes brittle and difficult to handle in the following top cell fabrication steps. Thus, we limit the PDA to 300 °C as the highest annealing temperature in this study.

The sputter conditions also strongly influence the device performance. Sputter damage can occur due to particles with high kinetic energies impinging on the substrate surface, leading to defects at the interface or in the shallow bulk.[30,31] Plasma luminescence and deep UV radiation can also introduce damage even if a thin silicon layer shields the sensitive POLO/c-Si interface from particles.[32] Highly energetic particles and radiation are mainly produced directly opposite to the target's surface, where the substrate is usually placed. However, by moving the substrate laterally from the center of the plasma region below the target, we achieve three beneficial effects. First, the intensity of plasma luminescence and deep UV radiation on the substrate are mitigated. Second, only scattered particles arrive on the substrate, which previously collided with molecules of the process gases and lost part of their kinetic energy thermalizing to lower energies. Third, the path length between the substrate surface and target surface is increased, so that the chance of collisions of the particles is increased, while the mean free path length of the particles remains unchanged. Indeed, by changing the sputtering conditions from the standard process (substrate placed opposite to the target) to the described "soft" process (substrate placed laterally), the effect in tandem performance is evident, though the ITO film thickness is unchanged. The $J-V$ scan of the soft sputtered device (full pink line) shown in Figure 2b presents a considerably higher V_{OC} compared with that made with the standard process. The inset shows the statistical improvement for both FF and V_{OC} when using the soft sputtering process: FF increases by 5.5%$_{abs}$ and V_{OC} by about 60 mV.

The proof-of-principle 3 P tandem devices in this study use bottom cells with a planar, saw damage-etched front side to facilitate spin coating of the top cell. The rear side is also planar and has a contact layout typical for bifacial PERC$^+$ technology.[33] This design results in a rather low J_{SC} around 16.5 mA cm^{-2} for the tandem devices, which is limited by the current density $J_{Si,EQE}$ generated in the bottom cell, as calculated from the EQE measurements shown in **Figure 3**a (black dotted line). Texturing

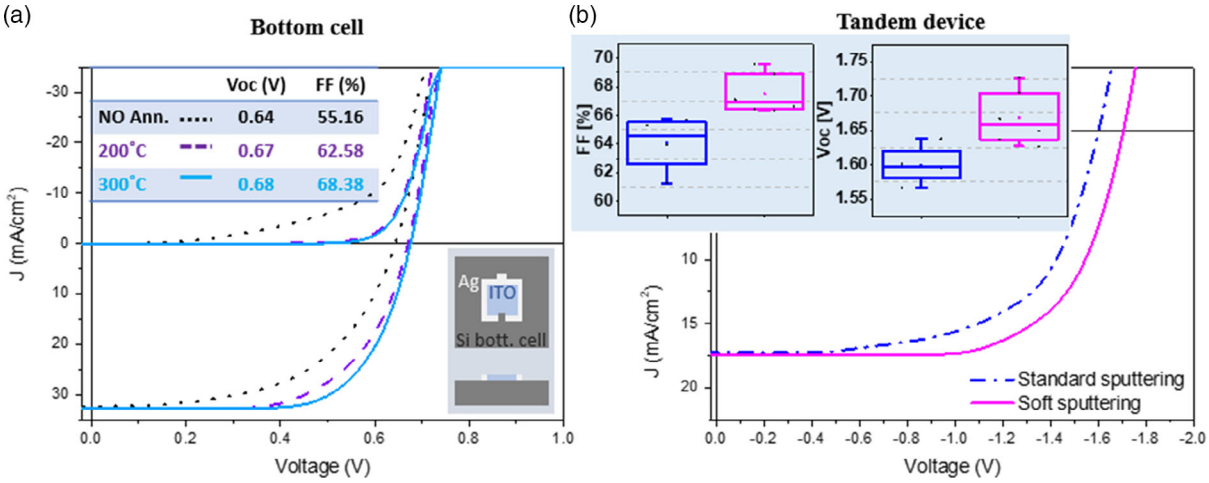


Figure 2. a) $J-V$ curves of a PERC/POLO/ITO/Ag bottom cell device with sputtered ITO (100 nm, recombination junction) as deposited and annealed at 200 and 300 °C, where 300 °C provides the highest FF and V_{OC}, as shown in the inset. b) $J-V$ curves of 3P tandem devices using standard and soft sputtering of the ITO recombination junction, demonstrating that soft sputtering increases the device V_{OC} and FF.

© 2022 The Authors. Solar RRL published by Wiley-VCH GmbH

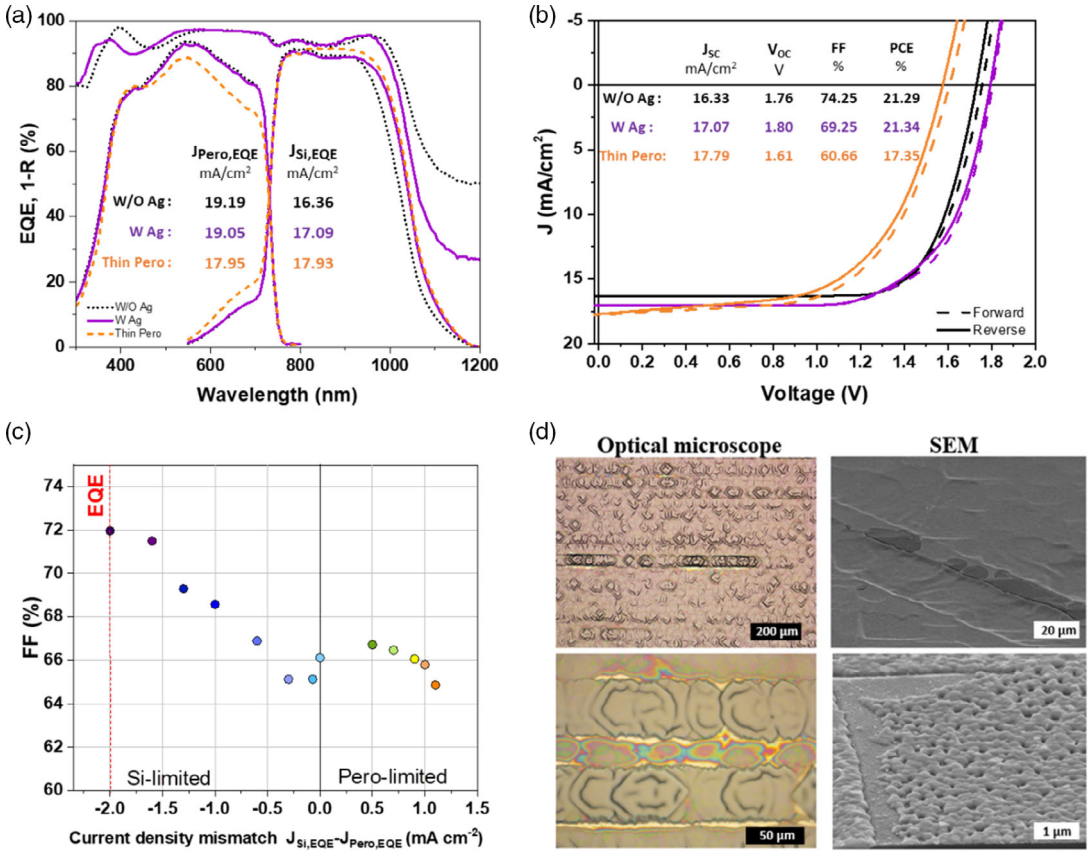


Figure 3. a) EQE and 1−*R* spectra and b) *J*−*V* curves of the perovskite−POLO−PERC tandem devices, showing comparison between samples without and with Ag back reflector and tandem device containing the thinner layer of the perovskite to achieve current matching conditions. c) Analysis of tandem devices showing importance of being current mismatched for obtaining higher FF values, blue dots correspond to measurement under a blue rich spectrum, and red data points to a red rich spectrum. d) Pictures obtained by optical microscopy (left) and SEM (right), showing coverage issues (absence of perovskite layer) at the edges of saw damage marks.

of the bottom cell front and/or rear side is a solution to improve tandem device performance by increasing the bottom cell's $J_{Si,EQE}$ contribution. We consider these options in optical simulations discussed later. To increase the current generation in the present bottom cells, we deposit 100 nm of Ag as a back reflector, thus changing from a bifacial to a monofacial cell design. Indeed, Figure 3a shows that the reflectance increases from 50% to above 70% at 1200 nm. This high reflectance induces a higher EQE in the bottom cell, in particular in the wavelength range from 930 to 1200 nm. Consequently, $J_{Si,EQE}$ increases by 0.7 mA cm^{-2} (Figure 3a, purple full line). The corresponding gain in J_{SC} of the tandem devices is observed in Figure 3b, which shows the *J*−*V* scans of the same device measured before and after deposition of the Ag back reflector. Next to the higher J_{SC}, a higher V_{OC} is measured with Ag back reflector. These values are in conjunction with a lower FF for the device with Ag back reflector, which is explained in detail in the next section. Thus, both tandem cell designs show very similar PCE values around 21.3%, which is the champion PCE of our 3 P tandem device until now and the first reported value for this particular tandem architecture. Statistics of the device parameters and maximum power point tracking (180 s) of optimized 3 P tandem devices are presented in Figure S2.3, Supporting Information.

The current density generated by the top cell also strongly affects the device performance. As mentioned earlier, the perovskite absorber used for the fabrication of the 3P tandem solar cells has a bandgap of 1.68 eV. As its thickness strongly influences the current density generated in the top cell, adapting its fabrication process is crucial to achieve current matching between the subcells. In particular, the standard spin-coating recipe uses a spin speed of 3500 rpm, which produces a perovskite layer of about 560 nm, resulting in a photocurrent $J_{Pero,EQE}$ of about 19.0 mA cm^{-2}. However, the bottom cell device only provides a $J_{Si,EQE}$ of 17.0 mA cm^{-2}. To reduce the current mismatch, we deposit a thinner perovskite layer by increasing the spin-coating speed to 5000 rpm resulting in a film thickness of about 470 nm. This reduces the top cell $J_{pero,EQE}$ to 18 mA cm^{-2}. While the J_{SC} of the top cell decreases, the J_{SC} of the bottom cell obviously increases, reaching also a $J_{Si,EQE}$ of 18 mA cm^{-2} (see orange dotted line in the EQE analysis shown in Figure 3a). Therefore, current matching is accomplished in this case. Figure 3b shows the *J*−*V* scan of the current-matched cell. Despite the increase in J_{SC}, the device PCE is reduced due to decreased V_{OC} and FF compared to the other *J*−*V* scans shown in the graph. Figure 3c shows the device FF for different current mismatch conditions obtained by intentionally modifying the

© 2022 The Authors. Solar RRL published by Wiley-VCH GmbH

light intensities of the incident spectrum in the red and blue wavelength regions, to influence the current generation of the bottom and top cells and with that the photocurrent mismatch, respectively. As reported in the study by Köhnen et al.,[34] for silicon bottom cell-limited conditions, the FF values decrease when changing from large current mismatch toward the current-matched situation. Under perovskite top cell-limited conditions, an increase in FF with increasing current mismatch is expected. In contrast, the FF of our 3P tandem solar cells does not show this increase once the perovskite cell becomes limiting for incident spectra containing less blue light, that is, being rich in red light. The highest FF value is therefore achieved in strongly silicon-limited devices, which are the conditions obtained using thicker perovskite films (560 nm) generating $J_{\mathrm{Pero,EQE}} = 19\ \mathrm{mA\,cm^{-2}}$ and $J_{\mathrm{Si,EQE}} = 17\ \mathrm{mA\,cm^{-2}}$, hence with $2\ \mathrm{mA\,cm^{-2}}$ current mismatch (as shown with the red vertical line in the mismatch graph in Figure 3c). The FF dependence on the current matching conditions is also demonstrated in Figure S2.4, Supporting Information. By changing the UV light intensity and measuring $J-V$ scans, highest FFs are achieved in strongly silicon cell-limited conditions, whereas lower FFs are obtained in current matching or perovskite-limited conditions. The dependence of the FF on the current mismatch condition also explains why the overall PCE of the device with Ag back reflector is similar to that of the device without the Ag back reflector (Figure 3b). While both J_{SC} and V_{OC} increase when adding the metallic layer on the back side, the FF decreases as the current mismatch between bottom and top cells reduces from $2.8\ \mathrm{mA\,cm^{-2}}$ without Ag to $2\ \mathrm{mA\,cm^{-2}}$ with Ag.

As mentioned earlier, in Figure 3c, the perovskite-limited part of the graph shows that moving toward larger current mismatch conditions does not improve the FF. This behavior points to a strong FF limitation in the perovskite top cell. To examine this, we investigate the perovskite layer with optical microscopy and SEM. The corresponding images are shown in Figure 3d. Optical microscopy images show defects positioned along horizontal lines on the surface, which are caused by the silicon wafer sawing process and remain visible on the bottom cell surface after saw damage etching. We find up to 3.5 µm-deep and 50 µm-wide grooves (see Figure S1.2, Supporting Information), which are still visible once the perovskite and all other layers of the top cell are deposited. In optical microscopy, we observe that in or at the border of these deep grooves, some areas show bright areas, suggesting that certain layers may be absent. SEM imaging confirms that the perovskite film does not uniformly cover these regions. This could be due to the limited edge coverage of the perovskite spin-coating process, as the step height on the wafer surface is much larger than the final film thickness. Another reason could be an incomplete coverage of the rough surface by the SAM. As SEM or optical microscopy cannot detect the presence of a SAM, we test this hypothesis using PTAA as an alternative HTL. In this case, we find even larger areas that are not covered by the perovskite. This suggests that it is not the presence or absence of the HTL that gives rise to perovskite-free regions, but rather the roughness of the bottom cell surface. In particular, the deep grooves with their rather steep edges hinder full coverage of the surface in spin coating of the perovskite. The large perovskite-free areas induce shunting, which strongly affects the tandem device performance, mainly by reducing FF and V_{OC}. The reason for this still relatively mild loss in FF despite the large areas not covered with perovskite might be the presence of the SnO_2 buffer layer, which is deposited on top of the C_{60} ETL. In the shunted areas, a stack of IZO/SnO_2/ITO/poly-Si forms the parallel current path. Considering the energy-level alignment of ITO and SnO_2,[35] it is possible that SnO_2 hinders carrier (electron) transport across this shunt path. Further, the high sheet resistance of the thin ITO and poly-Si limits the lateral transport through these layers, also reducing the impact of shunts. A similar decoupling effect was reported for nanocrystalline hydrogenated silicon films.[36]

Issues related to incomplete coverage on nonpolished surfaces can be avoided with conformal deposition methods like coevaporation.[37–42] Together with the successful application of SAMs (specifically, MeO-2PACz), this method has recently been applied to fabricate perovskite/silicon tandem cells using bottom cells with textured surfaces.[37] We regard the combination of conformal deposition methods and bottom cells with the textured front side as the most promising route toward the industrialization of the 3P tandem cell.

From the analysis earlier, we identify three major pathways for improving the tandem device performance: 1) increase the bottom cell photogeneration current by texturing, 2) optimize the bottom cell V_{OC} contribution to the tandem V_{OC}, and 3) enhance the top cell FF and V_{OC} by pinhole-free full coverage of the top cell absorber layer. In this section, we briefly discuss all three aspects and estimate their potential impact on the PCE of the perovskite–POLO–PERC tandem cell.

The bottom cells in this work are only 156 µm thin and have planar front and rear sides, that is, no light-trapping features. This limits the achievable J_{SC} due to reflection losses and incomplete absorption in the near-IR range. Optical simulations of the absorptance and reflectance match the measured EQE and reflectance spectra of our tandem cell, as shown in **Figure 4**. We provide details on the simulations in the supplemental information. The simulated top cell photocurrent density slightly underestimates the measured $J_{\mathrm{Pero,EQE}}$ due to a slightly lower absorptance in the wavelength region from 400 to 450 nm. The simulated bottom cell photocurrent is slightly higher than the experimental value as the simulated device has a higher absorptance in the wavelength region from 950 to 1100 nm.

The excellent agreement of the simulated and measured EQEs shows that the low J_{SC} in our devices is a result of the abovementioned optical limitations rather than recombination-induced J_{SC} losses, which are not included in the simulations. Starting from our parametrization for the both sides planar cell, the simulated data for a tandem device with a textured rear side results in a photocurrent density gain of $0.86\ \mathrm{mA\,cm^{-2}}$ in the bottom cell, while the photocurrent density in the top cell remains unchanged. Fine tuning the current matching would enable a tandem J_{SC} of $18.6\ \mathrm{mA\,cm^{-2}}$. Double-side texturing increases the photocurrent densities in both subcells and yields 19.65 and $19.41\ \mathrm{mA\,cm^{-2}}$ in the top and bottom cells, respectively, allowing for $19.5\ \mathrm{mA\,cm^{-2}}$ matched J_{SC}. An additional gain in J_{SC} is possible by reducing the parasitic absorption. This could be achieved by more transparent, high-mobility TCO materials.[43,44]

© 2022 The Authors. Solar RRL published by Wiley-VCH GmbH

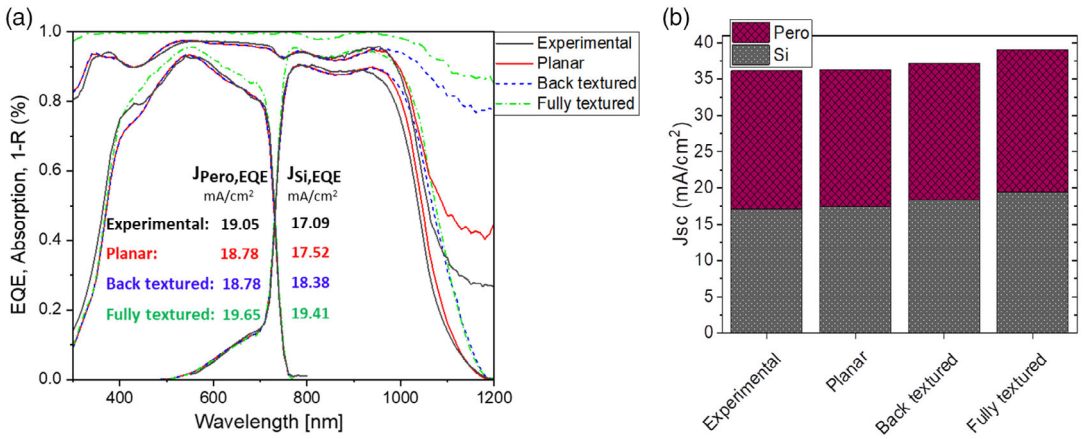


Figure 4. a) Measured EQE and (1−*R*) spectra of a double-side planar tandem cell (black lines). The simulated absorptance and (1−*R*) of the double-side planar device (red lines) match the experimental data. The dashed blue lines show the simulated data for a tandem device with a textured rear side. While the photocurrent density in the top cell remains unchanged, it increases by 0.86 mA cm^{-2} in the bottom cell. Results for double-side texturing are shown with dash-dotted green lines. The photocurrent densities increase to 19.65 and 19.41 mA cm^{-2} in the top and bottom cells, respectively. The inset shows values of $J_{Pero,EQE}$ and $J_{Si,EQE}$ for each condition. b) Column graph showing the total tandem current and contribution from top and bottom cell, for the experimental and simulated options (planar, back textured, and fully textured).

The main limitation for the bottom cell V_{OC} is carrier recombination at the locally diffused Al-p$^+$ regions. While test samples without rear contacts show minority carrier lifetimes of 1 ms after firing, samples with local Al-p$^+$ rear contacts only achieve 350 µs, as measured on full M2 wafers by ILM. The drop in minority carrier lifetime can be explained by the rather high carrier recombination at the local Al-p$^+$ contacts. Haase et al. investigated the effect of the area fraction of local Al-p$^+$ contacts formed in a similar process.[45] They identified the reduction of the Al-p$^+$ contact area fraction as an efficient way to improve the V_{OC} of p-type silicon IBC cells with n$^+$-POLO emitter and Al-p$^+$ base contacts up to 709 mV at an area fraction of 1%. They reached an even higher V_{OC} of 716 mV after further optimization of the contact geometry. In a tandem cell, the photocurrent is roughly halved compared with the situation in the study by Haase et al.[45]. Thus the optimum area fraction when balancing resistive and recombination losses should be even lower than in the single-junction application. In tandem operation, the roughly halved photogeneration in the silicon subcell also reduces the bottom cell V_{OC} contribution compared with the 1 sun situation in the study by Haase et al.[45]. We thus expect that a bottom cell V_{OC} contribution of 700 mV is feasible for our devices after optimizing the contact area fraction and the Al p$^+$ contact geometry.

Perovskite/silicon tandem devices with a very similar layer stack for the perovskite top cell, including the intermediate thin ITO layer, can achieve V_{OC} values of 1.9 V and FF of 80%, as demonstrated in champion devices.[3] The analysis of the subcell V_{OC} in the study by Al-Ashouri et al.[3] demonstrates that the perovskite top cell can contribute 1.2 V to the tandem V_{OC}. Together with the improved bottom cell rear contact geometry discussed earlier, we consider a V_{OC} potential of 1.9 V for a 3 P tandem device. Considering the pseudo-FF values obtained from the single-junction bottom cell characteristics (see Supporting Information for details), we expect that the POLO/PERC bottom cell would not limit the FF of the 3P tandem devices to values below 80%. Conformal perovskite deposition methods like coevaporation and the application of SAMs as lossless HTLs enable the fabrication of highly efficient perovskite/silicon tandem devices using front-side-textured bottom cells. Combining the V_{OC} of 1.9 V and the FF of 80% with the photocurrent generated for the fully textured device in our simulations, we estimate an efficiency potential of 29.5% for 3 P perovskite/silicon tandem devices first shown in this study. Note that further improvements through adjustments in the perovskite thickness and bandgap are not yet considered here. Messmer et al. found a maximum PCE of 30.1% in simulations of very similar tandem solar cells, including these additional optimizations, such as change of bandgap and layer thickness of the perovskite layer for closer current-matching conditions.[14]

4. Conclusion

We report on a proof-of-concept perovskite/silicon tandem solar cell with the high-temperature stable bottom cell featuring a passivating POLO front junction and a PERC rear side. For the bottom cell, we implement a process flow that is compatible with industrial, mainstream PERC technology. In particular, the active device area of our bottom cell features all industrially relevant components such as p-type Cz SDE base material, in situ n-type-doped poly-Si layers on a wet chemically grown interfacial oxide, a fired Al_2O_3/SiN_x rear side passivation, as well as screen-printed and alloyed Al-p$^+$ rear contacts. The top cell is then monolithically grown onto an ITO layer, which acts as the recombination junction. It is found that sputter damage is detrimental for the tandem performance and hence, particular care is taken during the ITO deposition, using the soft sputtered process and post-annealing treatment at 300 °C. Then, the perovskite top cell is fabricated using p−i−n junction device architecture, similar to top cells used previously for tandem devices built on SHJs. Integrating this subcell on the PERC/POLO bottom cell yields proof-of-concept tandem solar cells with up to 21.3% PCE.

© 2022 The Authors. Solar RRL published by Wiley-VCH GmbH

Based on our experimental findings and supporting optical simulations, we identify major process enhancements and estimate a PCE potential of 29.5%. This work paves the way for highly efficient perovskite/silicon tandem solar cells utilizing mainstream bottom cell technologies.

Supporting Information

Supporting Information is available from the Wiley Online Library or from the author.

Acknowledgements

This work was supported in part by the German Federal Ministry for Economic Affairs and Energy, under grant 03EE1017A&B (Project P3T), and in part by the Federal State of Lower Saxony. Additional funding was provided by the Helmholtz Association through the HySPRINT innovation lab project as well as by the Federal Ministry of Education and Research (BMBF) for funding of the Young Investigator Group Perovskite Tandem Solar Cells within the program "Materialforschung für die Energiewende" (grant no. 03SF0540). The optical simulations were performed at the Berlin Joint Lab for Optical Simulations for Energy Research (BerOSE) and the Helmholtz Excellence Cluster SOLARMATH of Helmholtz-Zentrum Berlin für Materialien und Energie, Zuse Institute Berlin and Freie Universität Berlin. The authors would like to thank H. Kohlenberg, G. Glowatzki, M. Turcu, and N. Mielich for bottom cell processing and R. Zieseniss for support with the confocal microscopy measurements at the Laboratory of Nano and Quantum Engineering, Leibniz University Hannover. The authors also thank Alvaro Tejada from HZB and Pontificia Universidad Católica del Perú for providing optical data.

Open access funding enabled and organized by Projekt DEAL.

Conflict of Interest

The authors declare no conflict of interest.

Data Availability Statement

The data that support the findings of this study are available from the corresponding author upon reasonable request.

Keywords

monolithic tandem solar cells, perovskite tandems, perovskite/silicon tandems, polycrystalline silicon on oxide/passivated emitter and rear cell tandems, recombination junctions

Received: December 17, 2021
Revised: January 26, 2022
Published online: February 17, 2022

[1] PV-Magazine, **2021**, https://www.pv-magazine.com/2021/08/31/chiles-renewables-auction-attracts-lowest-bid-of-0-01332-kwh/, (accessed: October 2021).
[2] B. Veith-Wolf, S. Schäfer, R. Brendel, J. Schmidt, *Sol. Energy. Mater. Sol. Cells* **2018**, *186*, 194.
[3] A. Al-Ashouri, E. Köhnen, B. Li, A. Magomedov, H. Hempel, P. Caprioglio, J. A. Márquez, A. B. Morales Vilches, E. Kasparavicius, J. A. Smith, N. Phung, D. Menzel, M. Grischek, L. Kegelmann, D. Skroblin, C. Gollwitzer, T. Malinauskas, M. Jošt, G. Matič, B. Rech, R. Schlatmann, M. Topič, L. Korte, A. Abate, B. Stannowski, D. Neher, M. Stolterfoht, T. Unold, V. Getautis, S. Albrecht, *Science* **2020**, *370*, 1300.
[4] Oxford PV, Press Release, **2020**. https://www.oxfordpv.com/news/oxford-pv-hits-new-world-record-solar-cell, (accessed: December 2021).
[5] NREL cell efficiency chart, https://www.nrel.gov/pv/cell-efficiency.html, (accessed: December, 2021).
[6] M. Jošt, L. Kegelmann, L. Korte, S. Albrecht, *Adv. Energy Mater.* **2020**, *10*, 1904102.
[7] J. P. Mailoa, C. D. Bailie, E. C. Johlin, E. T. Hoke, A. J. Akey, W. H. Nguyen, M. D. McGehee, T. Buonassisi, *Appl. Phys. Lett.* **2015**, *106*, 121105.
[8] J. Werner, A. Walter, E. Rucavado, S.-J. Moon, D. Sacchetto, M. Rienaecker, R. Peibst, R. Brendel, X. Niquille, S. De Wolf, P. Löper, M. Morales-Masis, S. Nicolay, B. Niesen, C. Ballif, *Appl. Phys. Lett.* **2016**, *109*, 233902.
[9] Y. Wu, D. Yan, J. Peng, T. Duong, Y. Wan, S. P. Phang, H. Shen, N. Wu, C. Barugkin, X. Fu, S. Surve, D. Grant, D. Walter, T. P. White, K. R. Catchpole, K. J. Weber, *Energy Environ. Sci.* **2017**, *10*, 2472.
[10] J. Zheng, C. F. J. Lau, H. Mehrvarz, F.-J. Ma, Y. Jiang, X. Deng, A. Soeriyadi, J. Kim, M. Zhang, L. Hu, X. Cui, D. S. Lee, J. Bing, Y. Cho, C. Chen, M. A. Green, S. Huang, A. W. Y. Ho-Baillie, *Energy Environ. Sci.* **2018**, *11*, 2432.
[11] J. Zheng, H. Mehrvarz, C. Liao, J. Bing, X. Cui, Y. Li, V. R. Gonçales, C. F. J. Lau, D. S. Lee, Y. Li, M. Zhang, J. Kim, Y. Cho, L. Granados Caro, S. Tang, C. Chen, A. W. Y. Ho-Baillie, *ACS Energy Lett.* **2019**, *4*, 2623.
[12] H. Shen, S. T. Omelchenko, D. A. Jacobs, S. Yalamanchili, Y. Wan, D. Yan, P. Phang, T. Duong, Y. Wu, Y. Yin, C. Samundsett, J. Peng, N. Wu, T. P. White, G. G. Andersson, N. S. Lewis, K. R. Catchpole, *Sci. Adv.* **2018**, *4*, eaau9711.
[13] VDMA, International Technology Roadmap for Photovoltaic (ITRPV), 12th ed., **2021**.
[14] C. Messmer, B. S. Goraya, S. Nold, P. S.C. Schulze, V. Sittinger, J. Schön, J. C. Goldschmidt, M. Bivour, S. W. Glunz, M. Hermle, *Prog. Photovolt. Res. Appl.* **2020**, 1.
[15] R. Peibst, M. Rienäcker, B. Min, C. Klamt, R. Niepelt, T. F. Wietler, T. Dullweber, E. Sauter, J. Hübner, M. Oestreich, R. Brendel, in IEEE, *Proc. WCPEC*, **2018**, p. 2635.
[16] R. Peibst, M. Rienäcker, B. Min, C. Klamt, R. Niepelt, T. F. Wietler, T. Dullweber, E. Sauter, J. Hübner, M. Oestreich, R. Brendel, *IEEE JPV* **2019**, *1*, 49.
[17] G. Nogay, F. Sahli, J. Werner, R. Monnard, M Boccard, M. Despeisse, F-J. Haug, Q. Jeangros, A. Ingenito, C. Ballif, *ACS Energy Lett.* **2019**, *4*, 84.
[18] C. Hollemann, M. Rienäcker, A. Soeriyadi, C. Madumelu, F. Haase, J. Krügener, B. Hallam, R. Brendel, R. Peibst, *Prog. Photovolt. Res. Appl.* **2022**, *30*, 49.
[19] K. Ramspeck, S. Reissenweber, J. Schmidt, K. Bothe, R. Brendel, *Appl. Phys. Lett.* **2008**, *93*, 102104.
[20] M. Wolf, H. Rauschenbach, *Adv. Energy Convers.* **1963**, *3*, 455.
[21] R. Peibst, Y. Larionova, S. Reiter, T. F. Wietler, N. Orlowski, S. Schäfer, B. Min, M. Stratmann, D. Tetzlaff, J. Krügener, U. Höhne, J.-D. Kähler, H. Mehlich, S. Frigge, R. Brendel, *IEEE J. Photovolt.* **2018**, *8*, 719.
[22] L. Tutsch, F. Feldmann, M. Bivour, W. Wolke, M. Hermle, J. Rentsch, *AIP Conf. Proc.* **2018**, *1999*, 040023.
[23] K. Tominaga, T. Yuasa, M. Kume, O. Tada, *Jpn. J. Appl. Phys.* **1984**, *23*, 936.
[24] K. Tominaga, T. Yuasa, M. Kume, O. Tada, *Jpn. J. Appl. Phys.* **1985**, *24*, 944.

© 2022 The Authors. Solar RRL published by Wiley-VCH GmbH

[25] A. Al-Ashouri, A. Magomedov, M. Roß, M. Jošt, M. Talaikis, G Chistiakova, T. Bertram, J. A. Márquez, E. Köhnen, E. Kasparavičius, S. Levenco, L. Gil-Escrig, C. J. Hages, R. Schlatmann, B. Rech, T. Malinauskas, T. Unold, C. Kaufmann, L. Korte, G. Niaura, V. Getautis, S. Albrecht, *Energy Environ. Sci.* **2019**, *12*, 3356.
[26] J. Xu, C. C. Boyd, Z. J. Yu, A. F. Palmstrom, D. J. Witter, B. W. Larson, R. M. France, J. Werner, S. P. Harvey, M. D. McGehee, *Science* **2020**, *367*, 1097.
[27] F. Lang, E. Köhnen, J. Warby, K. Xu, M. Grischek, P. Wagner, D. Neher, L. Korte, S. Albrecht, M. Stolterfoht, *ACS Energy Lett.* **2021**, *6*, 3982.
[28] M. De Bastiani, A. S. Subbiah, E. Aydin, F. H. Isikgor, T. G. Allen, S. De Wolf, *Mater. Horiz.* **2020**, *7*, 2791.
[29] Y. Larionova, H. Schulte-Huxel, B. Min, S. Hartmann, M. Turcu, T. Kluge, H. Mehlich, R. Brendel, R. Peibst, in *Proc. 36th EUPVSEC*, WIP, München, Germany **2019**, p. 172.
[30] K. Tominaga, M. Chong, Y. Shintani, *J. Vac. Sci. Technol., A* **1994**, *12*, 1435.
[31] W. Dewald, V. Sittinger, W. Werner, C. Jacobs, B. Szyszka, *Thin Solid Films* **2009**, *518*, 1085.
[32] B. Demaurex, S. De Wolf, A. Descoeudres, Z. C. Holman, C. Ballif, *Appl. Phys. Lett.* **2012**, *101*, 171604.
[33] T. Dullweber, C. Kranz, R. Peibst, U. Baumann, H. Hannebauer, A. Fülle, S. Steckemetz, T. Weber, M. Kutzer, M. Müller, G. Fischer, P. Palinginis, D. H. Neuhaus, *Progr. Photovolt. Res. Appl.* **2016**, *24*, 1487.
[34] E. Köhnen, M. Jošt, A. B. Morales-Vilches, P. Tockhorn, A. Al-Ashouri, B. Macco, L. Kegelmann, L. Korte, B. Rech, R. Schlatmann, B. Stannowski, S. Albrecht, *Sustain. Energy Fuels* **2019**, *3*, 1995.
[35] M. Stolterfoht, P. Caprioglio, C. M. Wolff, J. A. Márquez, J. Nordmann, S. Zhang, D. Rothhart, U. Hörmann, A. Redinger, L. Kegelmann, S. Albrecht, T. Kirchartz, M. Saliba, T. Unold, D. Neher, http://arxiv.org/abs/1810.01333, (accessed: October 2018).
[36] F. Sahli, B. A. Kamino, J. Werner, M. Bräuninger, B. Paviet-Salomon, L. Barraud, R. Monnard, J. P. Seif, A. Tomasi, Q. Jeangros, A. Hessler-Wyser, S. De Wolf, M. Despeisse, S. Nicolay, B. Niesen, C. Ballif, *Adv. Energy Mater.* **2017**, 1701609.
[37] M. Roß, S. Severin, M. B. Stutz, P. Wagner, H. Köbler, M. Favin-Lévêque, A. Al-Ashouri, P. Korb, P. Tockhorn, A. Abate, B. Stannowski, B. Rech, S. Albrecht, *Adv. Energy Mater* **2021**, *11*, 2101460.
[38] L. Gil-Escrig, M. Roβ, J. Sutter, A. Al-Ashouri, C. Becker, S. Albrecht, *Sol. RRL* **2021**, *5*, 2000553.
[39] C. Momblona, H. Kanda, A. A. Sutanto, M. Mensi, C. Roldán-Carmona, M. K. Nazeeruddin, *Sci. Rep.* **2020**, *10*, 10640.
[40] Y. Vaynzof, *Adv. Energy Mater.* **2020**, *10*, 2003073..
[41] Q. Guesnay, F. Sahli, C. Ballif, Q. Jeangros, *APL Mater.* **2021**, *9*, 100703.
[42] J. Li, H. Wang, X. Y. Chin, H. A. Dewi, K. Vergeer, T. W. Goh, J. Wei, M. Lim, J. Haur Lew, K. P. Loh, C. Soci, T. C. Sum, H. J. Bolink, N. Mathews, S. Mhaisalkar, A. Bruno, *Joule* **2020**, *4*, 1035.
[43] M. Morales-Masis, S. De Wolf, R. Woods-Robinson, J. W. Ager, C. Ballif, *Adv. Electron. Mater.* **2017**, *3*, 1600529.
[44] F. Sahli, J. Werner, B. A. Kamino, M. Bräuninger, R. Monnard, B. Paviet-Salomon, L. Barraud, L. Ding, J. J. Diaz Leon, D. Sacchetto, G. Cattaneo, M. Despeisse, M. Boccard, S. Nicolay, Q. Jeangros, B. Niesen, C. Ballif, *Nat. Mater.* **2018**, *17*, 820.
[45] F. Haase, B Min, C. Hollemann, J. Krügener, R. Brendel, R. Peibst, *Prog. Photovolt. Res. Appl.* **2021**, *29*, 516.

© 2022 The Authors. Solar RRL published by Wiley-VCH GmbH